Chapter 7
Curved Steel–Concrete-Steel Sandwich Shells Under Impact

7.1 Introduction

A curved steel–concrete-steel (CSCS) sandwich shell is composed of two curved steel plates, concrete core and shear connectors. It is developed to be mainly used in nuclear plants, offshore platforms, arctic caissons and protective structures (Ali et al. 2013; Hoff 1998; Huang and Liew 2016d; Huang et al. 2015b; Montague 1975) owing to its good mechanical performance. Meanwhile, the concrete debris will not spall outside when subjected to impact load owing to confinement provided by steel plates, which is suitable for protective structures (Mizuno et al. 2005).

Most of the existing studies were concentrated on the performances of SCS sandwich structures subjected to static load. To name a few, Yan et al. (2019a) conducted static experiments on CSCS sandwich shells under concentrated load. Lin et al. (2018 and 2019) explored the failure mechanisms of SCS beams through static tests, and their failure types were also identified. The extensive studies on the staftic performances of CSCS sandwich shells were also conducted (Yan et al. 2016a, b, c, 2019b; Yan and Zhang 2017). Huang and Liew (2016a, c) proposed the SCS wall and established an analytical model to calculate its resistance. Huang and Liew (2015a; 2016b) also carried out experimental, numerical and analytical studies on SCS panels with novel ultra-lightweight cement as core material. The flexure and shear performances of SCS slabs were also experimentally studied (Leng et al. 2015; Leng and Song 2017), and an analytical model was developed to predict their resistances.

However, the studies on impact behaviors of SCS sandwich structures (especially CSCS sandwich shells) are still limited. Liew et al. (2009) and Sohel et al. (2015) carried out experimental studies on SCS beams subjected to impact loading, and an analytical model was developed to predict their force–indentation relationships. In addition, Sohel and Liew (2014) also studied the impact behaviors of SCS sandwich slabs by employing experimental and analytical methods. Remennikov and Kong (2012) and Remennikov et al. (2013) conducted low-velocity impact tests on the axially-restrained SCS sandwich panels, and the corresponding Finite Element (FE) models were also established and validated against the test data. The responses of

SCS sandwich panels under drop-weight impact loading were experimentally and numerically studied (Zhao and Guo 2018; Zhao et al. 2018). Moreover, an analytical model was developed by Guo and Zhao (2019) for predicting displacement responses of the SCS sandwich panels under impact loading. With regard to the SCS sandwich panel under blast loading, its analytical model was developed and validated with the FE results (Wang et al. 2015, 2016b). Wang et al. (2016a) also experimentally studied the SCS sandwich panels under lateral pressure load, and the uniform pressure loading was achieved by employing an inflated airbag. However, all previous studies were focused on impact performances of SCS sandwich beams or panels, while limited works were carried out on impact performances of CSCS sandwich shells which had been proven to have superior performance under static loading (Huang et al. 2015b; Yan et al. 2016a, 2019a). Therefore, the impact performances of CSCS sandwich shells need to be studied to promote the application of such structure in resisting impact loading.

In this chapter, impact tests on nine CSCS sandwich shells were conducted by dropping a hammer with hemispherical head to obtain the impact force, displacement histories and failure modes. The effects of concrete thickness, steel plate thickness and spacing of shear connectors on the impact performances of CSCS sandwich shells were discussed. The FE models of CSCS sandwich shells were established and validated by comparing the FE-predicted impact force histories, displacement histories and failure modes with experimental results. In addition, an analytical model based on the equivalent single-degree-of-freedom (SDOF) method was proposed for predicting displacement responses of the CSCS sandwich shells under impact loading.

7.2 Test Program

7.2.1 Specimens

Nine CSCS sandwich shells were tested under drop-weight impact loading. Figure 7.1 illustrates the geometries of the specimens. The width (W), span (L), radius (R) and rise height (H) of all the nine specimens are 1200, 1200, 750 and 300 mm, respectively. High strength bolts with grade 8.8 were used as shear connectors in order to achieve strong composite action. The diameter of bolt was 12 mm. Four parameters were experimentally studied based on nine test specimens, including concrete thickness (70, 80 and 90 mm), steel plate thickness (2.87, 3.57 and 4.54 mm), thickness ratio of top to bottom steel plate (2.87–4.54 and 4.54–2.87 mm-mm) and spacing of shear connector (140, 200 and 260 mm), as shown in Table 7.1. The fabrication process of CSCS sandwich shells are given in Fig. 7.2. The steel plates were rolled into curved shape in the factory and welded to the end plates for forming the skeletons of CSCS shells. The bolts were installed through the holes reserved on the steel plates. Subsequently, the skeletons of CSCS shells were erected on the

Fig. 7.1 General illustration of the CSCS sandwich shell, reprinted from Yan et al. (2020a), copyright 2022, with permission from Elsevier
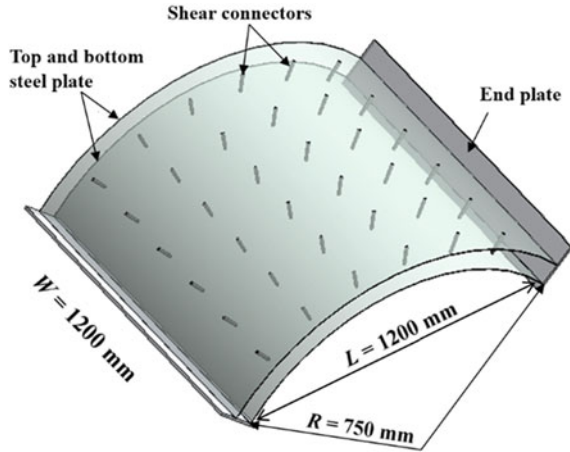

Table 7.1 Parameters of CSCS sandwich shells

Specimen	t_c (mm)	f_c (MPa)	t_{ts} (mm)	t_{bs} (mm)	f_y (MPa)	E_s (GPa)	S (mm)
CSCS3-70-3-200	70	32.73	2.87	2.87	350.32	209.27	200
CSCS3-80-3-200	80	32.73	2.87	2.87	350.32	209.27	200
CSCS3-90-3-200	90	32.73	2.87	2.87	350.32	209.27	200
CSCS4-70-4-200	70	32.73	3.57	3.57	307.28	206.70	200
CSCS5-70-5-200	70	32.73	4.54	4.54	332.70	215.61	200
CSCS3-70-5-200	70	32.73	2.87	4.54	350.32/332.70	209.27/215.61	200
CSCS5-70-3-200	70	32.73	4.54	2.87	332.70/350.32	215.61/209.27	200
CSCS3-70-3-140	70	32.73	2.87	2.87	350.32	209.27	140
CSCS3-70-3-260	70	32.73	2.87	2.87	350.32	209.27	260

Note t_c is concrete core thickness, t_{ts} is top steel plate thickness, t_{bs} is bottom steel plate thickness, f_c is compressive strength of concrete, f_y is yield strength of steel plate, E_s is elastic modulus of steel plate, and S is spacing of shear connector

ground, and concrete casting was implemented. After 28 days curing of the concrete, the fabrication of specimens was completed.

7.2.2 Materials

Q235 mild steel was employed for the skeletons of CSCS sandwich shells, including top and bottom steel plates as well as end plates (in Fig. 7.1). The material properties of mild steel were obtained through conducting tensile coupon tests. Table 7.1 shows the yield stress (f_y) and elastic modulus (E_s) of steel plates with different thicknesses. The unconfined compressive strength of concrete was 32.73 MPa, and its elastic

Fig. 7.2 Fabrication process: **a** rolling steel plates into curved shape, **b** erecting CSCS sandwich shells and **c** casting concrete, reprinted from Yan et al. (2020a), copyright 2022, with permission from Elsevier

modulus was 27.13 GPa. The yield and ultimate stress of bolt were 640 and 800 MPa, respectively.

7.2.3 Test Setup

The impact tests were carried out by utilizing a drop-weight impact test device, as shown in Fig. 7.3. The drop-weight impact test device is composed of a hammer with 100-mm-diameter hemispherical head, alterable counterweights (from 400 to 1000 kg) as well as a 600-kN force sensor which is installed between the hammer head and counterweights. The hammer weight (M) was 800 kg, and the drop height was 3 and 5 m, as given in Table 7.2.

CSCS sandwich shells were fixed to the triangular supports (refer to Fig. 7.3) via 18 bolts with diameter of 20 mm. The triangular supports were settled on the supporting beam (refer to Fig. 7.3) by 32 high strength bolts with diameter of 30 mm. All movements and rotations of the end plates of the CSCS sandwich shells are restrained by bolts to realize the fixed boundary condition. The high-speed camera was employed to capture the drop hammer with 2000 frames per second. In order to obtain the displacement histories of the bottom steel plate, two displacement transducers were used, and their layouts are shown in Fig. 7.4. The data logger TST5912 was used to record the impact forces and displacements.
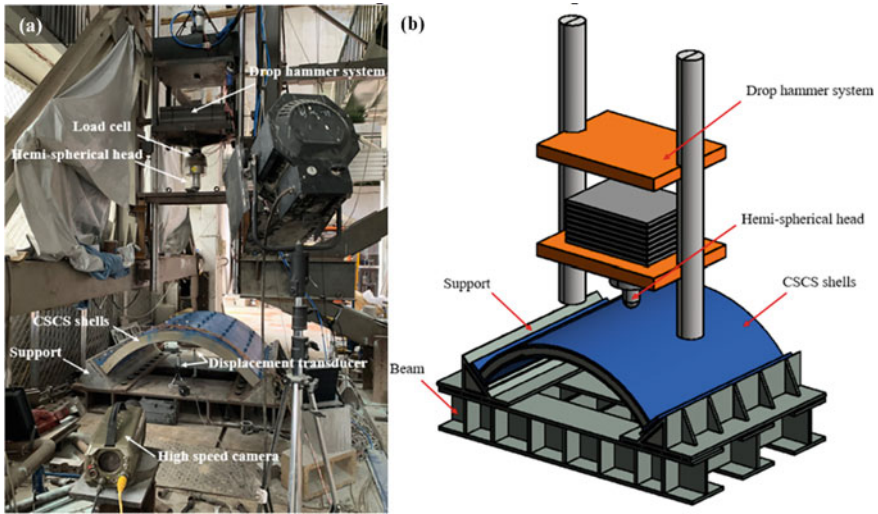
Fig. 7.3 Drop-weight impact test setup **a** photo and **b** 3D view, reprinted from Yan et al. (2020a), copyright 2022, with permission from Elsevier

7.3 Test Results and Discussions

Nine CSCS sandwich shells were tested against low-velocity impact loading. Eight specimens were subjected to the impact loading by dropping the hammer with drop height of 3 m. One specimen (CSCS3-70-3-260) was tested under the impact loading with drop height of 5 m to obtain the severe damage of the CSCS sandwich shell. Therefore, the effects of different parameters on impact performances of the CSCS sandwich shells were analyzed based on the former eight specimens with the same impact loading.

7.3.1 Damage Analysis of CSCS Shells

All specimens exhibited a deformation mode combined by local and global deformation. The central displacement of the bottom steel plate (D_b) was obtained by the displacement transducer WB2 (refer to Fig. 7.4). The displacement of the hammer (D_h) was measured by the high-speed camera.

The failure modes of all nine CSCS shells are dominated by local indentation and can be categorized into three types (refers to Fig. 7.5). Failure type I (plastic deformation of steel plate without fracture) occurred to specimen CSCS5-70-5-200, CSCS5-70-3-200 and CSCS3-70-3-140. Failure type II (fracture of top steel plate) occurred to specimen CSCS3-70-3-200, CSCS4-70-4-200 and CSCS3-70-5-200. Failure type

Table 7.2 Test parameters and results

Specimen	Drop height H (m)	Drop hammer weight M (kg)	Initial energy E_0 (kJ)	Inertial peak force F_I (kN)	Peak impact force F_p (kN)	D_{bmax} (mm)	D_{hmax} (mm)	Failure type
CSCS3-70-3-200	3	800	23.54	202.34	304.86	57.00	72.47	II
CSCS3-80-3-200	3	800	23.54	224.80	316.40	49.68	70.87	III
CSCS3-90-3-200	3	800	23.54	282.45	331.71	41.75	65.04	III
CSCS4-70-4-200	3	800	23.54	208.35	339.73	54.04	68.99	II
CSCS5-70-5-200	3	800	23.54	238.19	389.93	49.31	51.35	I
CSCS3-70-5-200	3	800	23.54	206.44	361.72	49.83	54.84	II
CSCS5-70-3-200	3	800	23.54	226.73	369.71	48.68	50.44	I
CSCS3-70-3-140	3	800	23.54	218.15	360.21	52.45	55.21	I
CSCS3-70-3-260	5	800	39.23	264.13	292.79	-	154.10	III

Note Failure type I means plastic deformation of steel plate without fracture, type II means fracture of top steel plate, and type III means penetration of top steel plate
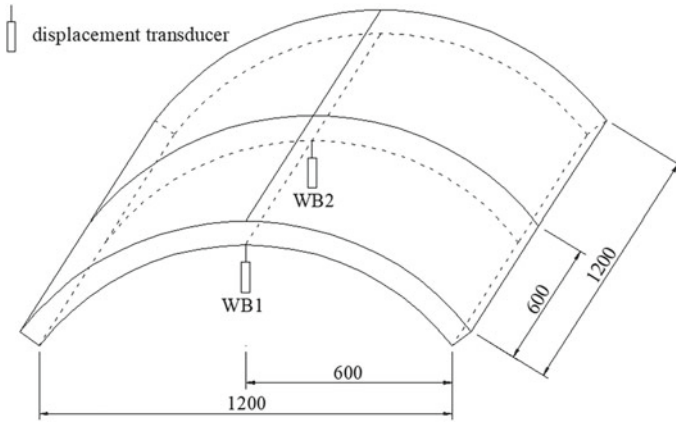
Fig. 7.4 Layout of displacement transducers, reprinted from Yan et al. (2020a), copyright 2022, with permission from Elsevier
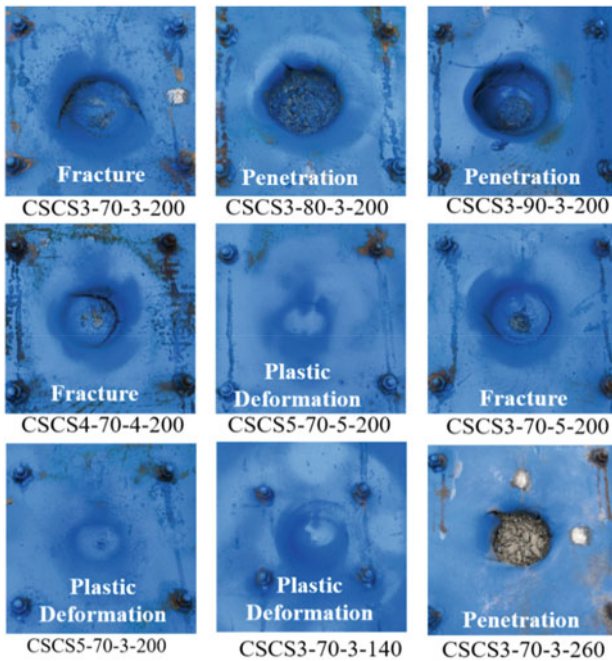

Fig. 7.5 Local deformation of top steel plate, reprinted from Yan et al. (2020a), copyright 2022, with permission from Elsevier
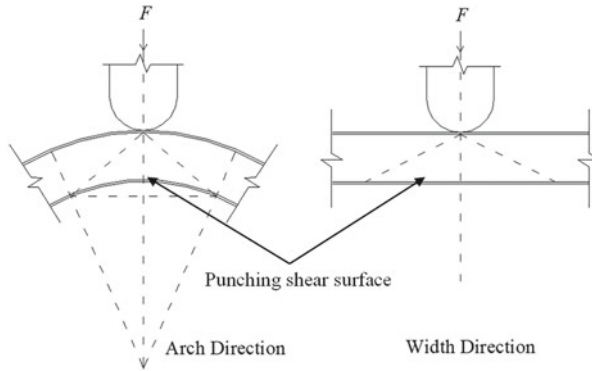
Fig. 7.6 Concrete punching shear failure, reprinted from Yan et al. (2020a), copyright 2022, with permission from Elsevier

III (penetration of steel plate) was observed for specimen CSCS3-80-3-200, CSCS3-90-3-200 and CSCS3-70-3-260. With thicker top steel plate and smaller spacing of shear connectors, the impact resistance and composition action of specimens were improved, which resulted in minor damage of the CSCS shell (Failure type I). This is because the thicker steel plate improved the punching shear resistance of the CSCS sandwich shell, which has been proved in former studies (Yan et al. 2019a, 2016a). The failure mode of the CSCS sandwich shell subjected to low-velocity impact load is similar to that under static concentrated load, i.e., initial punching shear failure and subsequent membrane stretching of steel plates (Yan et al. 2019a). When the deformation was small, the steel plate and concrete core resisted impact force together, as illustrated in Fig. 7.6. In this stage, concrete core was the main contributor to the impact resistance. After the concrete core was punched, the membrane stretching of the top steel plate mainly contributed to the impact resistance. The concrete could still offer some impact resistance, as the bottom steel plate provided confinement to the concrete core (refers to Fig. 7.7). Thus, the thicker steel plate resulted in higher impact resistance of the CSCS shell. The impact resistance of the CSCS shell would be decreased as the decease of top steel plate thickness. Thus, the failure damage

Fig. 7.7 Membrane stretching of steel plate, reprinted from Yan et al. (2020a), copyright 2022, with permission from Elsevier
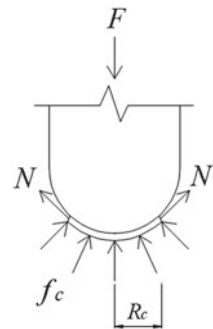
became more serious, which was fracture of the top steel plate in this test. However, if the spacing of shear connectors was too large, the composition action of the CSCS shell would be weakened, leading to the most serious failure type (penetration of top steel plate). Meanwhile, the thicker concrete core could enhance the impact resistance of the CSCS shell (i.e., higher impact force and smaller displacements of both bottom steel plate and hammer), but could result in the most serious failure type owing to reduced local deformation zone. The reason is that thicker concrete core resulted in higher stiffness of the CSCS shell, which could reduce the indentation of concrete core near the periphery of drop hammer and lead to smaller area of local deformation. Moreover, thicker concrete core resulted in smaller deformation of steel plates, which can be seen from Table 7.2 that both D_h and D_b decreased with increasing thickness of concrete core. Figure 7.8 shows the global deformation of the CSCS shells with typical three failure types after impact tests. The permanent global deformation (D_g) was measured by the displacement transducer WB1 (refers to Fig. 7.4). It shows that the D_g of the specimens with three failure types were small (i.e., the ratio of global deformation to local deformation is less than 9.9% for all the tested specimens). The specimen with more serious failure type had smaller area of local deformation and global deformation. For thicker concrete core and thinner steel plates, the impact energy was mainly absorbed by the shear failure of concrete and fracture of top steel plate. While for thicker steel plates, the fracture of top steel plate was prevented, and thus the impact energy dissipated by global deformation was relatively higher.

Figure 7.9a shows the impact force and displacement histories of specimen CSCS5-70-5-200 with failure type I. The impact process is composed of three stages, i.e., inertial stage, loading stage and unloading stage (Zhao and Guo 2018). The inertial stage occurred in the first 2 ms. The drop hammer and the CSCS sandwich shell contacted during inertial stage, resulting in the local impact zone of the shell being forced to move downwards with the same velocity of the drop hammer. Thus, the impact force increased rapidly to a peak value. However, the significant change of impact force at this stage was induced by inertial effect and could not represent the actual load carrying capacity of the CSCS shell (Zhao and Guo 2018). The impact force vibrated after the inertial peak. Meanwhile, the central displacement of the bottom steel plate (D_b) and hammer displacement (D_h) increased rapidly. The loading stage occurred from 2 to 13 ms for specimen CSCS5-70-5-200. The drop hammer and CSCS sandwich shell moved together with the impact force increasing in this stage owing to the increasing resistance of the CSCS shell via membrane stretching of the top steel plate. When the specimen reached its maximum displacement, the impact force also achieved to its maximum value which was called peak impact force (F_p). The impact force in this stage could generally represent the load carried by the CSCS shell. The local deformation zone was continuously expanding to achieve an increasing membrane resistance of the shell. The concrete core was also crushed, and partial impact force was transferred to the bottom steel plate through the concrete core and shear connectors. The loading stage finished as the velocity of the hammer reduced to zero. The unloading stage occurred from 13 to 23 ms for CSCS5-70-5-200. In this stage, the energy stored in the CSCS shell started to decrease. The impact

Fig. 7.8 Global deformation
of three failure types (D_g is
global deformation): **a**
CSCS5-70-5-200, **b**
CSCS3-70-3-200, **c**
CSCS3-80-3-20, reprinted
from Yan et al. (2020a),
copyright 2022, with
permission from Elsevier
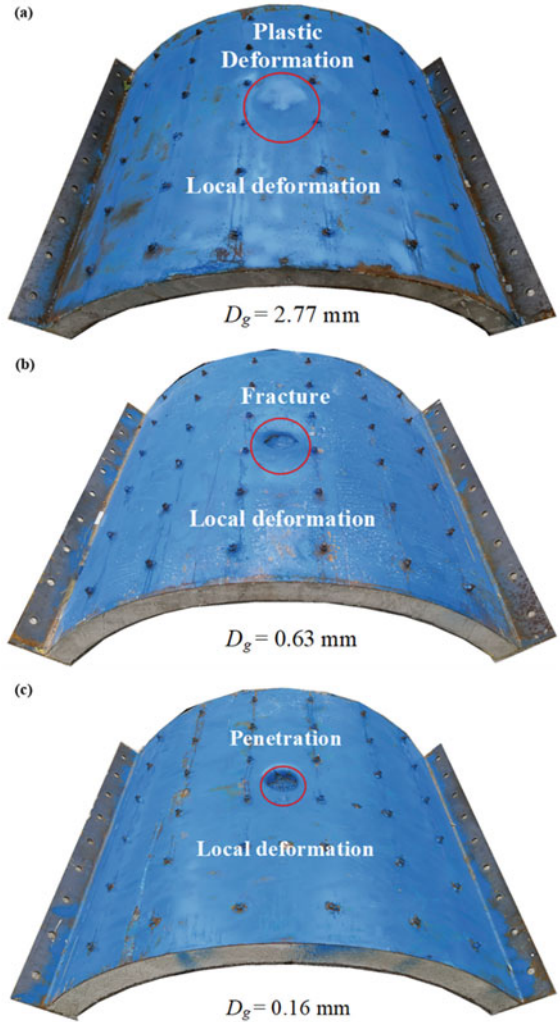
force would drop down to zero after the hammer rebounded, and the D_b recovered
to a stable value. The two steel plates deformed together to resist impact load, and
therefore the values of D_h and D_b showed same trend. However, almost constant
difference between D_h and D_b during impact process observed in Fig. 7.9a was due
to the local indentation.

As for the impact force and displacement histories of specimen CSCS3-70-3-
200 with failure type II in Fig. 7.9b, three stages during impact process can also be
observed, similar to the specimens with failure type I. However, the steel plate started
to fracture at 6 ms during loading stage, which led to a sudden drop of impact force
(refer to Fig. 7.9b). At this moment, the hammer still went downwards, while the

Fig. 7.9 Impact force and central displacement histories for specimens with different failure types: **a** CSCS5-70-5-200, **b** CSCS3-70-3-200, **c** CSCS3-80-3-200, reprinted from Yan et al. (2020a), copyright 2022, with permission from Elsevier
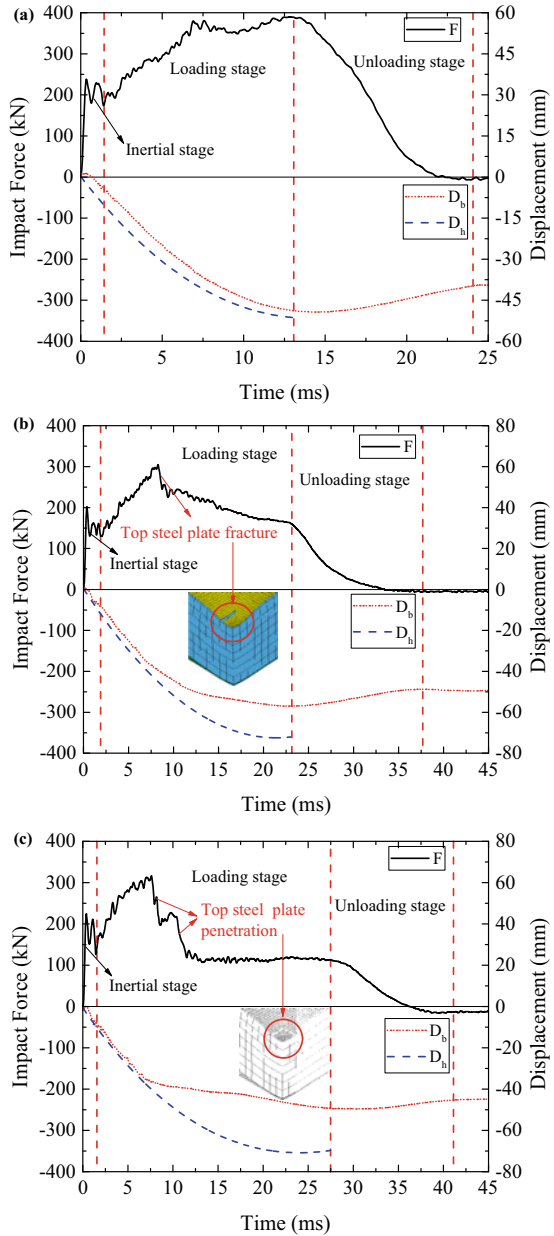
impact force monotonically decreased because of the continuous fracture of the top steel plate. When the displacement reached to the maximum value, the velocity of the hammer reduced to zero, and the loading stage finished. The difference between D_h and D_b was stable before fracture of the top steel plate. After that, slower increase of D_b as compared to D_h was observed, which could be attributed to the reduced impact energy transferred to the bottom steel plate after fracture of the top steel plate, i.e., partial impact energy originally dissipated by the bottom steel plate before fracture was dissipated by concrete and top steel plate.

Figure 7.9c shows the impact force and displacement histories of specimen CSCS3-80-3-200 with failure type III, and similar three stages during impact process can also be observed. However, the top steel plate was penetrated by the hammer (6–12 ms in Fig. 7.9c), which led to the drop of impact force from the peak value to a stable value. At this moment, the hammer continuously moved downwards, while the impact force remained a stable value. This stable impact resistance was provided by the concrete core below the hammer head, which was confined by surrounding concrete and bottom steel plate. The difference between D_h and D_b remained stable before penetration of the top steel plate. After that, slower increase of D_b was seen, and the difference between D_h and D_b after penetration was more significant as compared to failure type II, which was due to more portion of impact energy dissipated by penetration of the top steel plate and subsequent crushing of concrete.

7.3.2   Impact Force History

Figure 7.10 depicts impact force–time histories of eight specimens under the same impact loading, and the influences of concrete core thickness, steel plate thickness, thickness ratio of top to bottom steel plate and spacing of shear connectors were discussed as follows.

Figure 7.10a shows the influences of concrete core thickness (70, 80, and 90 mm) on impact force histories. The variation of concrete core thickness showed little effect on peak impact force (increased from 304.86 to 316.40 kN and 331.71 kN). However, by increasing the thickness of concrete core, the failure type was shifted from fracture of the top steel plate to penetration, resulting in more serious damage. The reason is that thicker concrete core resulted in smaller area of local deformation and more serious damage of the top steel plate. Yan et al. (2019a) have observed the similar behaviors in the former studies on CSCS shells under concentrated load applied in a quasi-static manner. Generally, the inertial peak force is affected by impact velocity, mass and contact stiffness. The impact velocity and mass were same for the eight specimens, and therefore only contact stiffness affects the inertial peak force in this test. Figure 7.10a shows that thicker concrete core can enhance the contact stiffness, leading to the higher inertial peak force from 202.34 kN to 224.80 and 282.45 kN (improved by 11.1% and 39.6%).

Figure 7.10b shows the effect of steel plate thickness (2.87, 3.57 and 4.54 mm) on impact force histories. By increasing steel plate thickness from 2.87 to 3.57 and
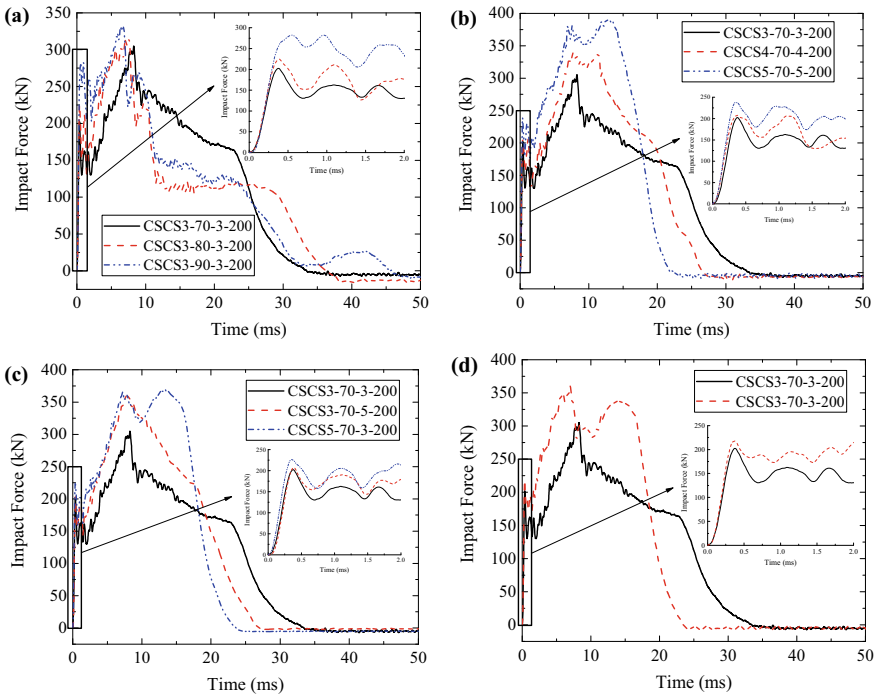
Fig. 7.10 Comparison of impact force histories for specimens: **a** concrete core thickness, **b** steel plate thickness, **c** top to bottom steel plate thickness ratio and **d** spacing of shear connectors, reprinted from Yan et al. (2020a), copyright 2022, with permission from Elsevier

4.54 mm, the peak impact force was improved from 304.86 to 339.73 and 389.93 kN, respectively (improved by 10.2% and 27.9%). Meanwhile, the damage of CSCS shell could be mitigated, as "plastic deformation of steel plate without fracture" occurred to CSCS5-70-5-200 with thickest steel plate. The thicker steel plate means higher strength, which resulted in higher impact force of the CSCS shell during loading stage. Moreover, the thicker steel plate could dissipate more impact energy and resulted in less damage of the CSCS shell. Increasing thickness of steel plate also enhanced contact stiffness, leading to higher inertial peak force from 202.34 to 208.35 kN and 238.19 kN (improved by 3.0 and 17.7%).

Figure 7.10c depicts the influence of thickness ratio of top-to-bottom steel plate on impact force. Both CSCS3-70-5-200 and CSCS5-70-3-200 (with same total thickness of top and bottom steel plates, but different thickness ratio) exhibited the similar peak impact force, but the failure types of them were different. No fracture was observed for specimen CSCS5-70-3-200 with thicker top steel plate. However, fracture of the top steel plate occurred to specimen CSCS3-70-5-200. The inertial peak force showed in Fig. 7.10c indicates that increasing top steel plate thickness could enhance the contact stiffness, and therefore the higher inertial peak force was observed for specimen CSCS5-70-3-200 as compared to CSCS3-70-5-200. Increasing bottom steel plate

thickness could also enhance the contact stiffness, but showed less enhancement as compared to increasing top steel plate.

Figure 7.10d presents the effect of spacing of shear connectors on impact force. The decrease of spacing from 200 to 140 mm resulted in the increase of peak impact force from 304.86 to 360.21 kN (increased by 18.2%) owing to the enhanced composition action of the CSCS shell. The top and bottom steel plates as well as shear connectors worked together to resist the impact force during the loading stage, and smaller spacing of shear connectors could improve the contribution of the bottom steel plate to impact resistance of the CSCS shell. Figure 7.10d also shows that decreasing spacing of shear connectors can increase the inertial peak force from 202.34 to 218.15 kN (improved by 7.8%). This is mainly because the contact stiffness can be enhanced with higher composition action.

7.3.3 Displacement History and Permanent Deformation

The central displacement histories of the bottom steel plate (D_b) of eight specimens are shown in Fig. 7.11. Increasing the concrete core thickness is found to reduce the maximum displacement of the bottom steel plate, as shown in Fig. 7.11a, i.e., the maximum displacement is reduced from 57.00 mm to 49.68 and 41.75 mm, respectively (decreased by 12.8 and 26.75%). This is mainly because both the stiffness and resistance of the specimen are enhanced by increasing thickness of concrete core. The influence of steel plate thickness on D_b is plotted in Fig. 7.11b. By increasing steel plate thickness from 2.87 mm to 3.57 and 4.54 mm, the maximum displacement decreases from 57.00 mm to 54.04 and 49.31 mm (decreased by 5.2% and 13.5%). The increased steel plate thickness can also improve the resistance and stiffness of the CSCS shell, which led to the reduction of maximum displacement. This phenomenon could also be observed from Fig. 7.11c. The summed thickness of top and bottom steel plates for specimen CSCS3-70-5-200 and CSCS5-70-3-200 were the same, and thus the maximum displacement of them were similar and higher than that of CSCS3-70-3-200 with smaller summed thickness. However, the thicker top steel plate showed higher resistance and stiffness, which resulted in slightly lower maximum displacement (48.68 mm for CSCS5-70-3-200 and 49.83 mm for CSCS3-70-5-200). Figure 7.11d depicts the effect of spacing of shear connectors on D_b. By decreasing the spacing of shear connectors, the maximum displacement was reduced from 57.00 mm to 52.45 mm (decreased by 8.7%) owing to the higher composition action of the CSCS shell.

Figure 7.12 plots the permanent deformations of the CSCS shells along arch and width directions. The deformations of top steel plates were obtained by using a laser ranging device after impact tests. The intervals were 10 mm within the impact area (a 200-mm-diameter circle) and 50 mm out of the impact area. The local deformation of the CSCS shell was more obvious while the global deformation occupied only a little part of the whole deformation. For the tested CSCS sandwich shells with thicker concrete core and thinner steel plates, the impact energy was mainly absorbed by
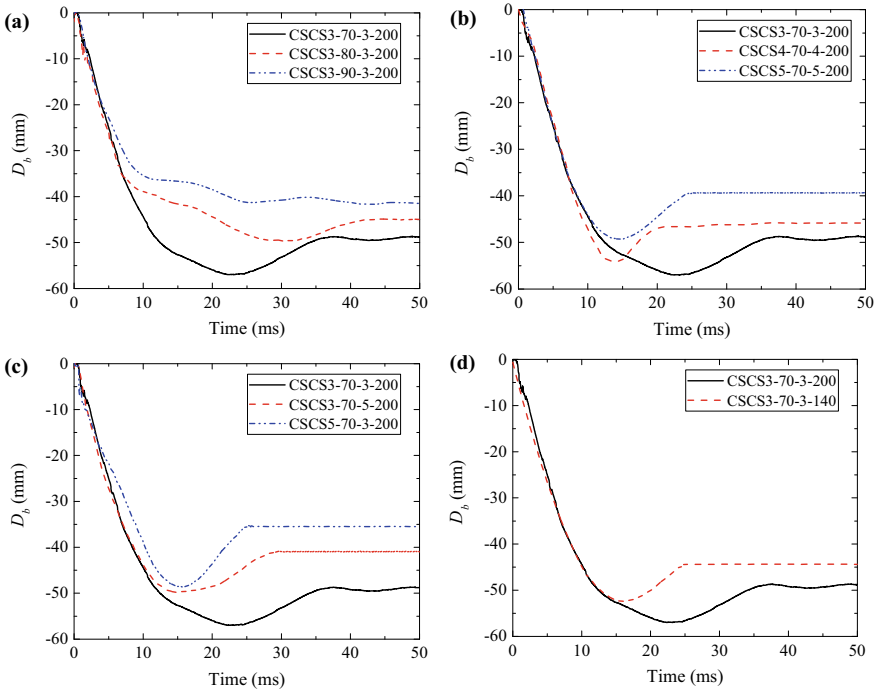
Fig. 7.11 Comparison of central displacement history of bottom steel plate for specimens: **a** concrete core thickness, **b** steel plate thickness, **c** top to bottom steel plate thickness ratio and **d** spacing of shear connectors, reprinted from Yan et al. (2020a), copyright 2022, with permission from Elsevier

fracture of the top steel plate as well as shear failure of concrete. While for the CSCS sandwich shells with thicker steel plates, the fracture of the top steel plate was prevented, and thus relatively more impact energy was dissipated through global deformation.

7.4 Numerical Modeling

7.4.1 FE Model Establishment

The FE analysis was conducted based on LS-DYNA, and quarter FE model of the CSCS shell under drop-weight impact loading was established, as shown in Fig. 7.13. The concrete core and drop hammer were modeled with an eight-node brick element, combined with reduced integration. In order to simulate steel plates, Belytschko-Tsay shell element was employed. Hughes-Liu beam element was employed for modeling shear connectors. Yan et al. (2019a) have obtained the optimal mesh sizes for the
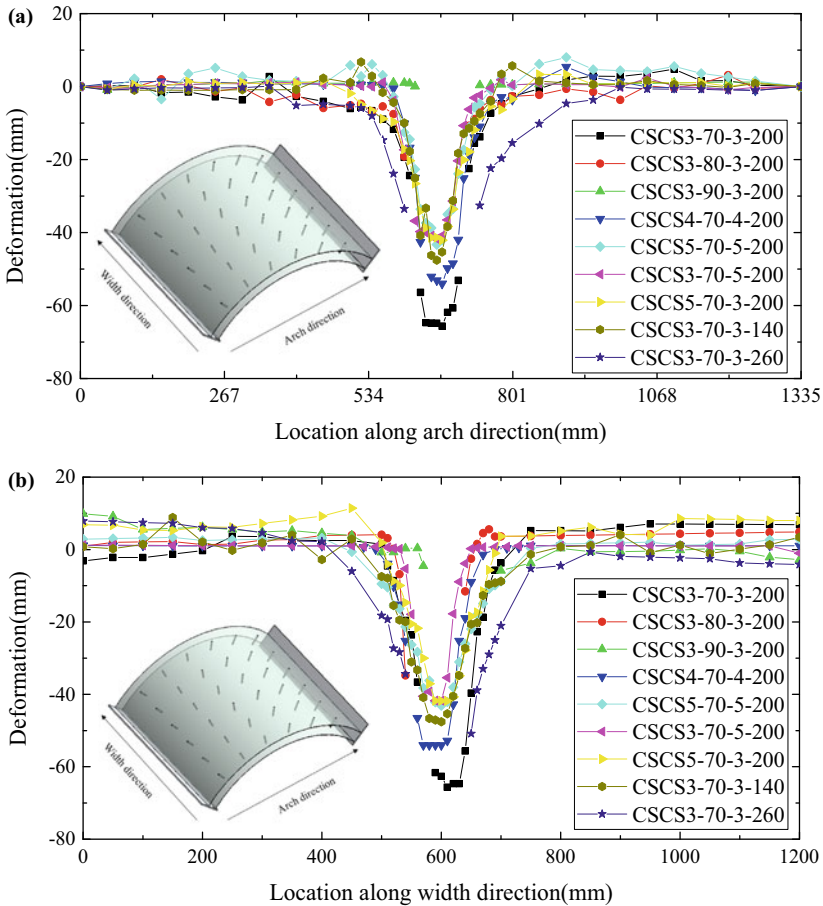
Fig. 7.12 Permanent deformation of the top steel plate along **a** arch direction and **b** width direction, reprinted from Yan et al. (2020a), copyright 2022, with permission from Elsevier

CSCS shell in order to achieve both accurate FE-predictions and less computing time as follows: 2×2 mm^2 mesh size for steel plates in the impact zone and 30×30 mm^2 at the edge of the shell; $10 \times 10 \times 10$ mm^3 for concrete core; 10 mm for shear connectors.

In order to simulate concrete core under impact load with both accuracy and efficiency, the Continuous Surface Cap (CSC) material model in LS-DYNA (Hallquist 2006) was adopted. This model was developed by US Federal Highway Administration (FHWA 2007) and widely used in recent years to model concrete under dynamic loading. Meanwhile, the users can obtain the default parameters for ordinary concrete by inputting basic parameters, including unconfined compressive strength, density and maximum aggregate size. Piecewise Linear Plasticity (PLP) material model was
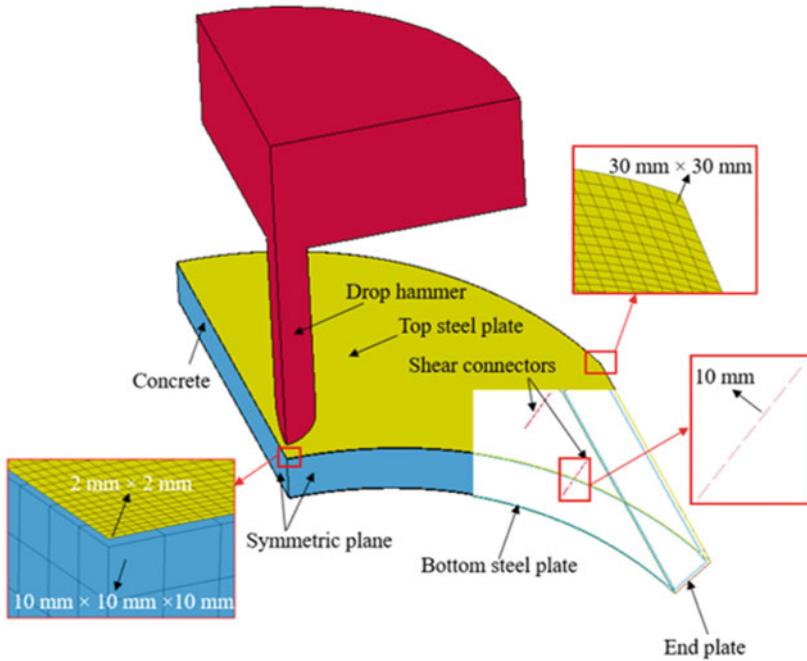
Fig. 7.13 Quarter FE model, reprinted from Yan et al. (2020a), copyright 2022, with permission from Elsevier

employed to model steel plates and shear connectors. The users can define the stress–strain relationship and failure strain according to their tensile coupon test data. In this study, the true stress–effective plastic strain relationships for the steel plates with different thicknesses were given in Fig. 7.14. The failure strain was defined as 0.2 for failure type II and III, i.e., the element with effective plastic strain exceeding

Fig. 7.14 True stress–effective plastic strain curves for steel plates, reprinted from Yan et al. (2020a), copyright 2022, with permission from Elsevier
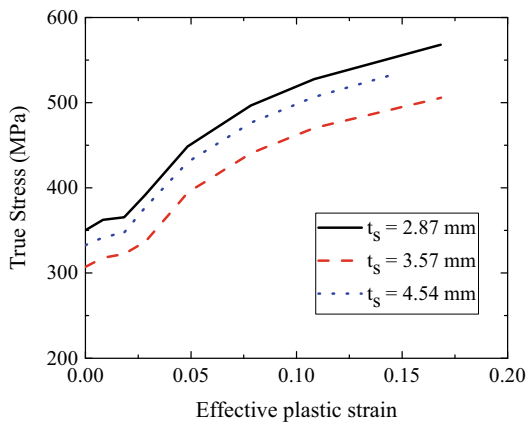
0.2 will be removed from the FE calculation. The strain rate effect was taken into consideration by using the Cowper-Symonds model, and the strain rate parameters C and P were $802 \, \text{s}^{-1}$ and 3.585 (Abramowicz and Jones 1986). The Plastic Kinematic (PK) material model was applied for simulating the hammer.

By constraining the displacements and rotations of nodes on the end plate, the fixed boundary can be achieved in the FE model. In order to simulate the contacts between two parts, automatic surface to surface contact algorithm was adopted. Both static and dynamic coefficient of friction applied in the contact pairs were 0.2. *Contact_Tiebreak_Nodes_to_Surface in LS-DYNA was adopted to simulate the connections between bolts and steel plates. The input strength was the ultimate strength of one bolt. Yan et al. (2019a) have confirmed its applicability in the former study.

7.4.2 FE Results and Discussions

The comparisons of central displacement of the bottom steel plate (D_b) and impact force histories between FE simulations and tests are shown in Figs. 7.15 and 7.16. Table 7.3 gives the results between FE-predictions and tests. Figure 7.15 shows that the value of D_b reached to a maximum value and then recovered to a stable value, which was matched with the test results. Meanwhile, the FE model can also provide accurate predictions on the hammer displacement (D_h), as shown in Table 7.3. The impact force predicted by the FE model are also composed of three stages (i.e., inertial, loading and unloading stage), which can be seen from Fig. 7.16. The impact force histories show good agreement with the test results. Figure 7.17 depicts the different failure types of the specimens between tests and FE simulations. The FE model can accurately predict three failure types observed from the tests. The average FE-to-test ratio for impact force is 1.143 with a coefficient of variation of 0.065. The FE model overestimates the maximum value of D_b by 5.7% with a coefficient of variation of 0.040. While the maximum value of D_h is underestimated by the FE model by 5.2% with a coefficient of variation of 0.145. Based on the comparisons between the FE-predictions and tests in terms of impact force histories, central displacement of the bottom steel plate histories, hammer displacement histories and failure types, the accuracy of the FE model can be validated. The slight differences between the FE-predictions and test results may be attributed to the geometric imperfections of the fabricated specimens. Another possible reason is that the impact velocity inputted in the FE model may be slightly different from the actual impact velocity in the test owing to the existence of friction between the drop-weight system and guild rails.

Figure 7.18 shows the internal energies of the top steel plate, concrete core, and bottom steel plate of the specimens with typical three failure types (CSCS5-70-5-200, CSCS3-70-3-200 and CSCS3-80-3-200). The majority of the impact energy was dissipated by concrete core (72.9–75.6%), followed by top steel plate (18.0–19.9%) and bottom steel plate (6.4–7.4%). This also proved that concrete core was the main part to dissipate impact energy because of the shear failure of concrete (refers to
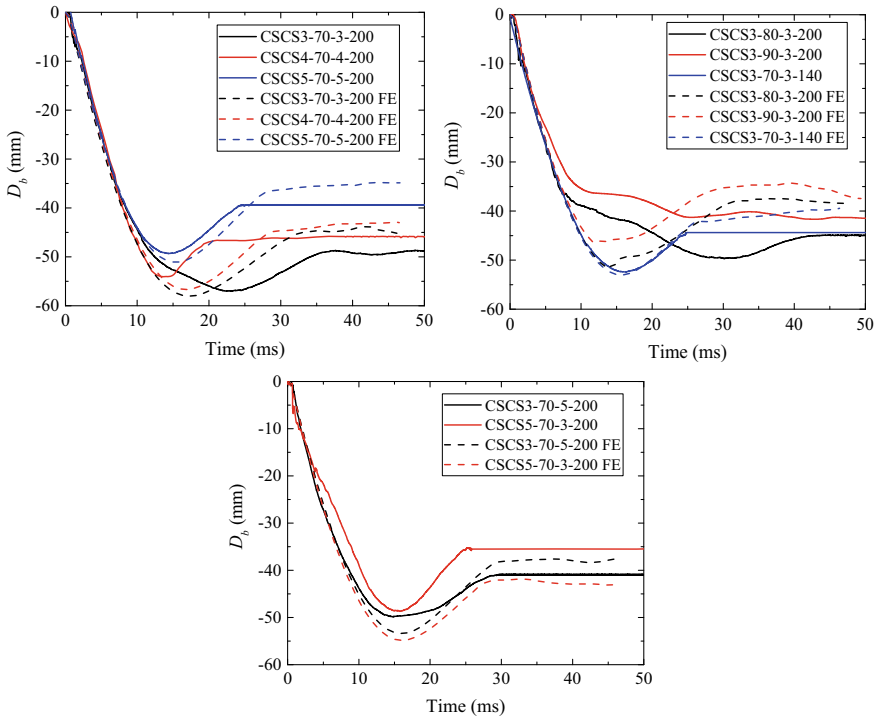
Fig. 7.15 Comparison of central displacement of bottom steel plate histories between FE and experiments, reprinted from Yan et al. (2020a), copyright 2022, with permission from Elsevier

Fig. 7.6). After shear failure of concrete, the steel plate was the main part to resist impact force. However, the concrete core can still absorb the majority of the impact energy owing to the confinement provided by the bottom steel plate.

7.5 Analytical Model

7.5.1 Force–Displacement Relationship

Figure 7.19 presents the impact force–displacement curves of three CSCS sandwich shells obtained from the impact tests, and they can be approximately divided into two stages, i.e., elastic and plastic stage, as shown in Fig. 7.20. Therefore, a bilinear curve can be used to represent the impact force–displacement relationship of the CSCS sandwich shell.
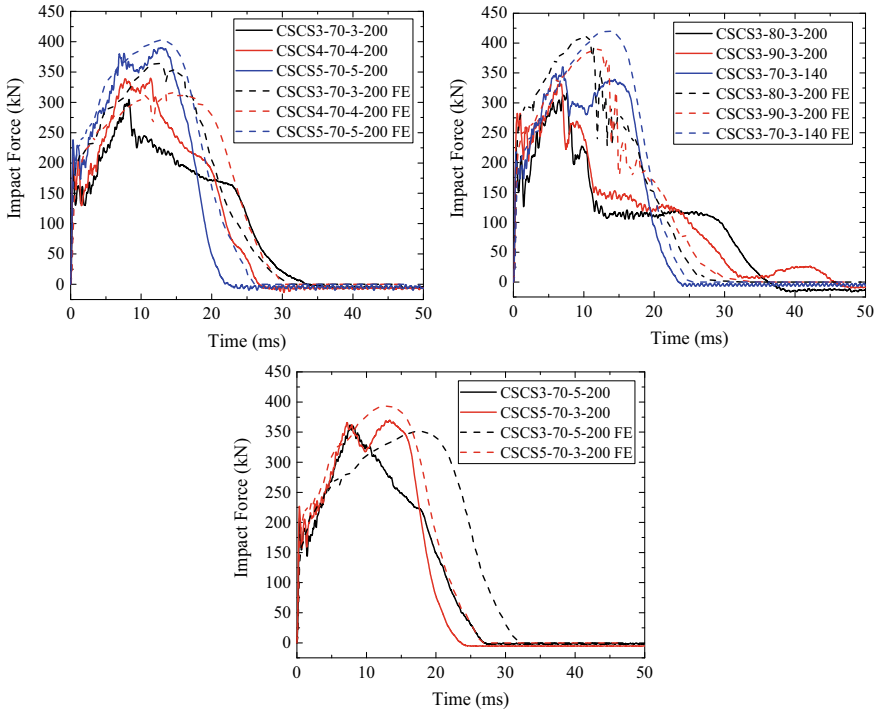
Fig. 7.16 Comparison of impact force between FE and experiments, reprinted from Yan et al. (2020a), copyright 2022, with permission from Elsevier

7.5.1.1 Elastic Stage

The calculation of the force–displacement relationship in elastic stage is based on the principle of minimum potential energy. The strain energy of the steel plate induced by membrane stretching was given in the theory of plates and shells (Timoshenko and Woinowsky-Krieger 1959):

$$V_s = \frac{E_s t_s}{1 - v^2} \int_0^{2\pi} \int_0^a \left(\varepsilon_r^2 + \varepsilon_\theta^2 + 2v\varepsilon_r\varepsilon_\theta \right) r\, dr\, d\theta \tag{7.1}$$

where v is Poisson's ratio, E_s is elastic modulus of the steel plate, t_s is thickness of the steel plate, ε_r is the radial strain, and ε_θ is the circumferential strain.

Sohel and Liew (2014) gave the equations for the radial displacement as well as the values of C_1 and C_2,

$$u(r) = r(a - r)(C_1 + C_2 r) \tag{7.2}$$

Table 7.3 Comparison of experiments and FE-predictions

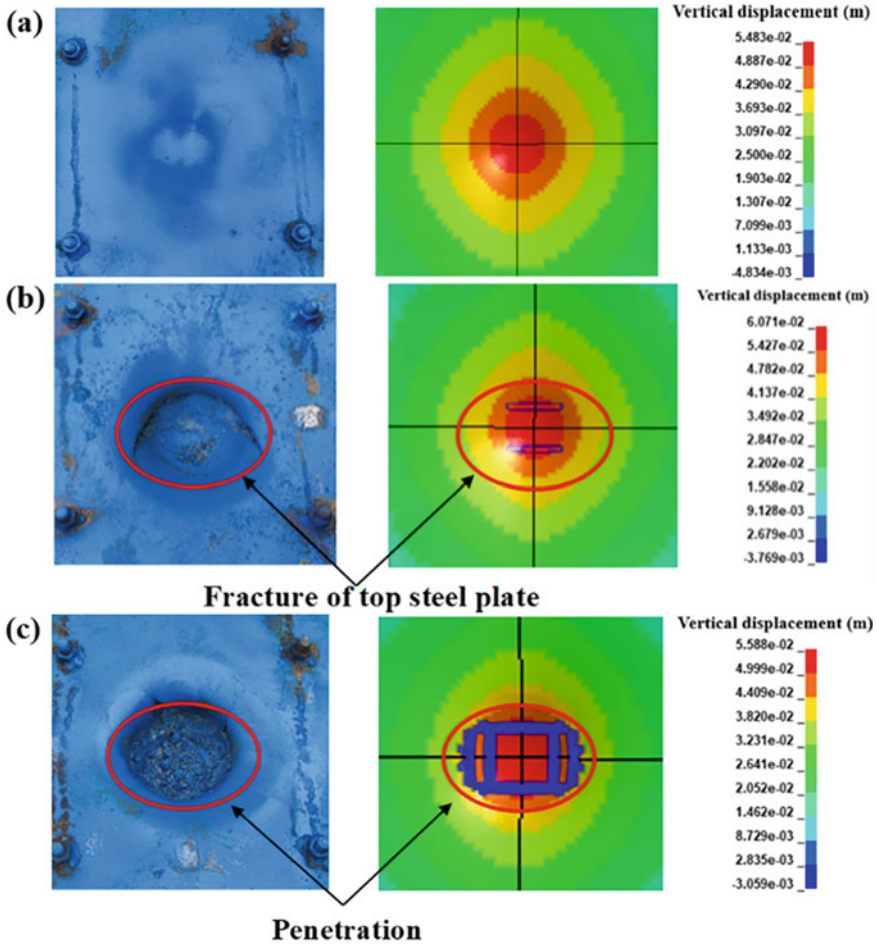| Specimen	Peak impact force F_p (kN)	Peak impact force F_{pFE} (kN)	$\frac{F_{pFE}}{F_p}$	D_{bmax} (mm)	D_{bmaxFE} (mm)	$\frac{D_{bmax\,FE}}{D_{b\,max}}$	D_{hmax} (mm)	D_{hmaxFE} (mm)	$\frac{D_{hmax\,FE}}{D_{h\,max}}$
CSCS3-70-3-200	304.86	365.10	1.198	57.00	57.99	1.017	72.47	61.20	0.844
CSCS3-80-3-200	316.40	391.23	1.237	49.68	51.57	1.038	70.87	55.88	0.788
CSCS3-90-3-200	331.71	411.75	1.241	41.75	46.42	1.112	65.04	51.79	0.796
CSCS4-70-4-200	339.73	378.10	1.113	54.04	56.67	1.049	68.99	60.01	0.870
CSCS5-70-5-200	389.93	402.38	1.032	49.31	51.07	1.036	51.35	54.84	1.068
CSCS3-70-5-200	361.72	393.64	1.088	49.83	53.36	1.071	54.84	57.56	1.050
CSCS5-70-3-200	369.71	393.09	1.063	48.68	54.83	1.126	50.44	57.38	1.138
CSCS3-70-3-140	360.21	420.87	1.168	52.45	53.01	1.011	55.21	56.69	1.027
CSCS3-70-3-260	292.79	335.88	1.147	–	–	–	–	–	–
Average			1.143			1.057			0.948
Cov			0.065			0.040			0.145

Fig. 7.17 Comparison of failure types between FE and experiments: **a** no fracture, **b** fracture of top steel plate and **c** penetration, reprinted from Yan et al. (2020a), copyright 2022, with permission from Elsevier

$$C_1 = 0.596084 \frac{\delta^2}{a^3}; \, C_2 = -1.50127 \frac{\delta^2}{a^4} \tag{7.3}$$

Thus, the strain energy of the steel plate can be expressed as:

$$V_s = \frac{3.5014\pi \, E_s t_s \delta^4}{12(1 - v^2)a^2} \tag{7.4}$$

The work done by concrete can be expressed as:

Fig. 7.18 Internal energy of
different parts s: **a**
CSCS5-70-5-200, **b**
CSCS3-70-3-200, **c**
CSCS3-80-3-200, reprinted
from Yan et al. (2020a),
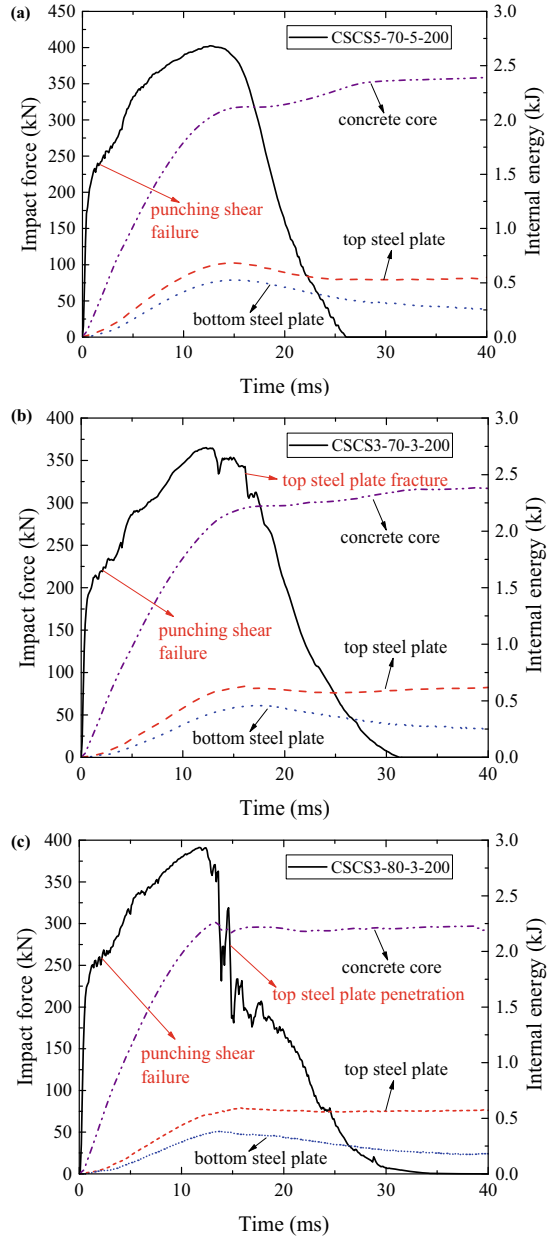copyright 2022, with
permission from Elsevier

Fig. 7.19 Impact
force–displacement curves
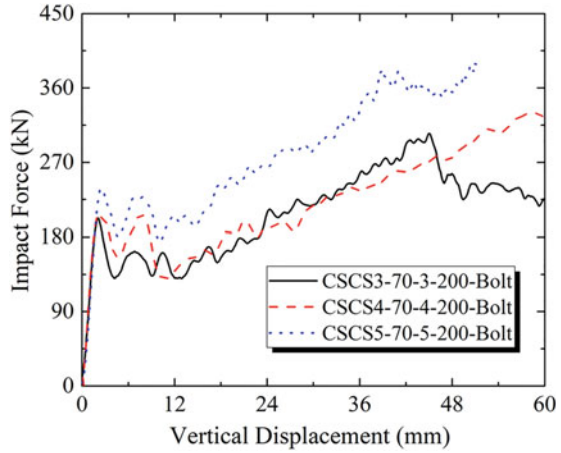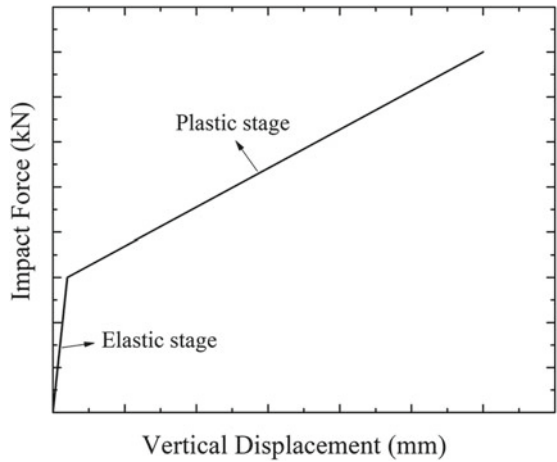of CSCS shells under impact
loading

Fig. 7.20 Simplified curve
for impact
force–displacement relation
of the CSCS shell

$$V_{con} = \int_0^{\delta} F_{con}d\delta = \frac{\pi a^2 E_c \delta^2}{10t_c} \qquad (7.5)$$

where t_c and E_c are the thickness and elastic modulus of the concrete core, respectively. On the basis of the principle of minimum potential energy, the partial derivative of the total potential energy with respect to the vertical displacement (δ) is obtained, i.e., the relationship between the impact force, vertical displacement, and the size of local deformation (a) is obtained as follows:

$$F = \frac{1.28\pi E_s t_s \delta^3}{a^2} + \frac{\pi a^2 \delta E_c}{5t_c} \qquad (7.6)$$

Minimalizing F with respect to a leads to the following equation:

$$a^2 = 2.53\sqrt{\frac{E_s t_s t_c}{E_c}}\delta \qquad (7.7)$$

Substituting Eq. (7.7) into Eq. (7.6), the relationship between the impact force and vertical displacement is obtained as follows:

$$F=3.18\sqrt{\frac{E_s t_s E_c}{t_c}}\delta^2; k_e = \frac{F_y}{\delta_y} \qquad (7.8)$$

Equation (7.8) also defines the elastic stiffness, which is the ratio of the nominal yield strength (F_y) to the corresponding vertical displacement (δ_y). The F_y can be calculated according to the formulae developed by Yan et al. (2020b), and the δ_y can be calculated based on the relationship between the force and vertical displacement obtained in Eq. (7.8).

7.5.1.2 Plastic Stage

Table 7.4 summarizes the elastic stiffness and plastic stiffness of the three CSCS shells tested by Yan et al. (2020b). It can be found that the average ratio of plastic stiffness to elastic stiffness was 0.109. The impact force–displacement curve of the specimen under impact loading is similar to the load–displacement curve under quasi-static loading (Yan et al. 2020a). Therefore, it is assumed that the ratio of plastic stiffness to elastic stiffness is 0.11, as given in Eq. (7.9).

$$k_p = 0.11 k_e \qquad (7.9)$$

Table 7.4 Stiffness in elastic and plastic stage obtained from static tests

Specimen	k_e (kN/mm)	k_p (kN/mm)	k_p / k_e
CSCS3-70-3-200-Bolt	19.55	2.207	0.113
CSCS4-70-4-200-Bolt	29.96	2.914	0.097
CSCS5-70-5-200-Bolt	30.68	3.628	0.118

7.5.2 *Displacement Response*

7.5.2.1 Equation of Motion

The calculation of the displacement response of the CSCS shell under impact loading is based on SDOF method. As shown in Fig. 7.21, the CSCS shell under drop-weight impact can be equivalent to a SDOF model, and its equation of motion is expressed as:

$$(m_e + m_h)\ddot{\delta} + c\dot{\delta} + R(\delta) = 0 \tag{7.10}$$

where m_e and c are the effective mass and damping of the CSCS shell, respectively, and m_h is the mass of the hammer.

The CSCS shell is a structural member with continuous mass distribution. To convert the continuously distributed mass into an equivalent concentrated mass, two assumptions are employed as follows: (1) The displacement of the mass in the SDOF model is same to vertical displacement of the CSCS shell; (2) The kinetic energy of the mass in the SDOF model is same to kinetic energy of the CSCS shell. Figure 7.21a presents the shape function $\varphi(x, y)$ of the CSCS shell. The deformation of the CSCS shell at any point can be obtained based on the shape function when the central displacement of the shell is known. The effective mass (m_e) can be obtained in Eq. (7.11) based on the second assumption:

$$\frac{1}{2}m_e\dot{\delta}^2 = \iint \frac{1}{2}m(x, y)\left[\dot{\delta}\varphi(x, y)\right]^2 dxdy \tag{7.11}$$

The permanent deformation shape of the CSCS shell was measured after the impact test, based on which the shape function is given as:
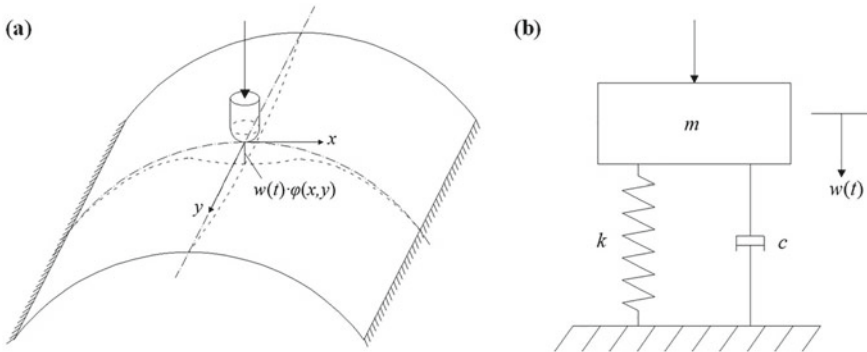

Fig. 7.21 Analytical model: **a** CSCS shell and **b** SDOF system

$$\varphi(x, y) = \left(1 - \frac{x^2}{2.53\sqrt{\frac{f_y E_s t_s t_c}{f_c E_c}}\delta}\right)^4 \left(1 - \frac{y^2}{6.48\sqrt{\frac{f_y E_s t_s t_c}{f_c E_c}}\delta}\right)^4$$

$$|x| \le \sqrt{2.53\sqrt{\frac{f_y E_s t_s t_c}{f_c E_c}}\delta}, |y| \le \sqrt{6.48\sqrt{\frac{f_y E_s t_s t_c}{f_c E_c}}\delta} \tag{7.12}$$

where f_y is the yield stress of the steel plate, f_c is the cylindrical compressive strength of the concrete. The effective mass of the CSCS shell can be written as:

$$m_e = \iint m(x, y)[\varphi(x, y)]^2 dx dy \tag{7.13}$$

The damping has little effect on the impact response of the CSCS shell during the loading stage. Hence, the damping can be ignored, and the damping coefficient (c) is adopted as 0 during the loading stage. However, the damping should be considered during the unloading stage as the free vibration amplitude decreases rapidly. The damping coefficient (c) is adopted as $2\sqrt{m_e k}$ during the unloading stage.

The equation of motion (Eq. 7.10) can be calculated based on finite difference method. The initial conditions of the equation of motion can be expressed as:

$$\delta(0) = 0$$
$$\dot{\delta}(0) = \frac{m_h}{m_e + m_h} v_0 \tag{7.14}$$

The displacement, velocity and acceleration of the SDOF system at time t_i can be given as:

$$\delta(t_i) = \delta_i$$
$$\dot{\delta}(t_i) = \dot{\delta}_i = \frac{\delta_{i+1} - \delta_i}{\Delta t}$$
$$\ddot{\delta}(t_i) = \ddot{\delta}_i = \frac{\delta_{i+2} - 2\delta_{i+1} + \delta_i}{(\Delta t)^2} \tag{7.15}$$

where Δt is the time step, and Eq. (7.10) can be written as:

$$(m_e + m_h)\frac{\delta_{i+2} - 2\delta_{i+1} + \delta_i}{(\Delta t)^2} + c\frac{\delta_{i+1} - \delta_i}{\Delta t} + R(\delta_i) = 0 \tag{7.16}$$

The displacement of the SDOF system at time t_{i+2} can be obtained as:

$$\delta_{i+2} = 2\delta_{i+1} - \delta_i - \frac{c\Delta t}{m_e + m_h}(\delta_{i+1} - \delta_i) - \frac{(\Delta t)^2}{m_e + m_h}R(\delta_i) \tag{7.17}$$

when $i = 0$ and 1 (i.e., $t = 0$ and Δt), the displacement of the SDOF system can be given as:

$$\delta(0) = 0$$

$$\delta(\Delta t) = \delta(0) + \dot{\delta}(0)\Delta t = \frac{m_h}{m_e + m_h}v_0\Delta t \tag{7.18}$$

Based on Eqs. (7.17) and (7.18), the displacement–time history of the CSCS shell can be obtained through iterative calculations.

7.5.2.2   Validation with Experimental Results

Figure 7.22 shows the comparison of the impact force–displacement curves obtained from tests and analytical-predictions, and good agreement between them can be observed. The observed differences in the elastic stages can be attributed to the inertial effect which is not considered in the analytical model and also exhibits little effect on the displacement response of the CSCS shell. Figure 7.23 shows the comparison of the displacement–time histories obtained from tests and analytical-predictions.
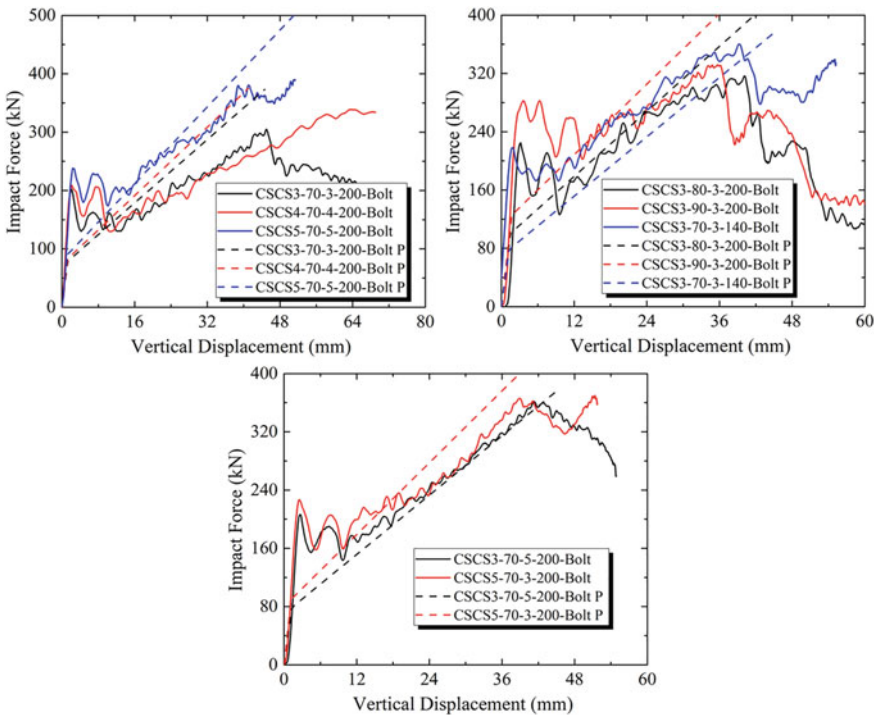

Fig. 7.22 Comparison of impact force–vertical displacement curves between tests and predictions
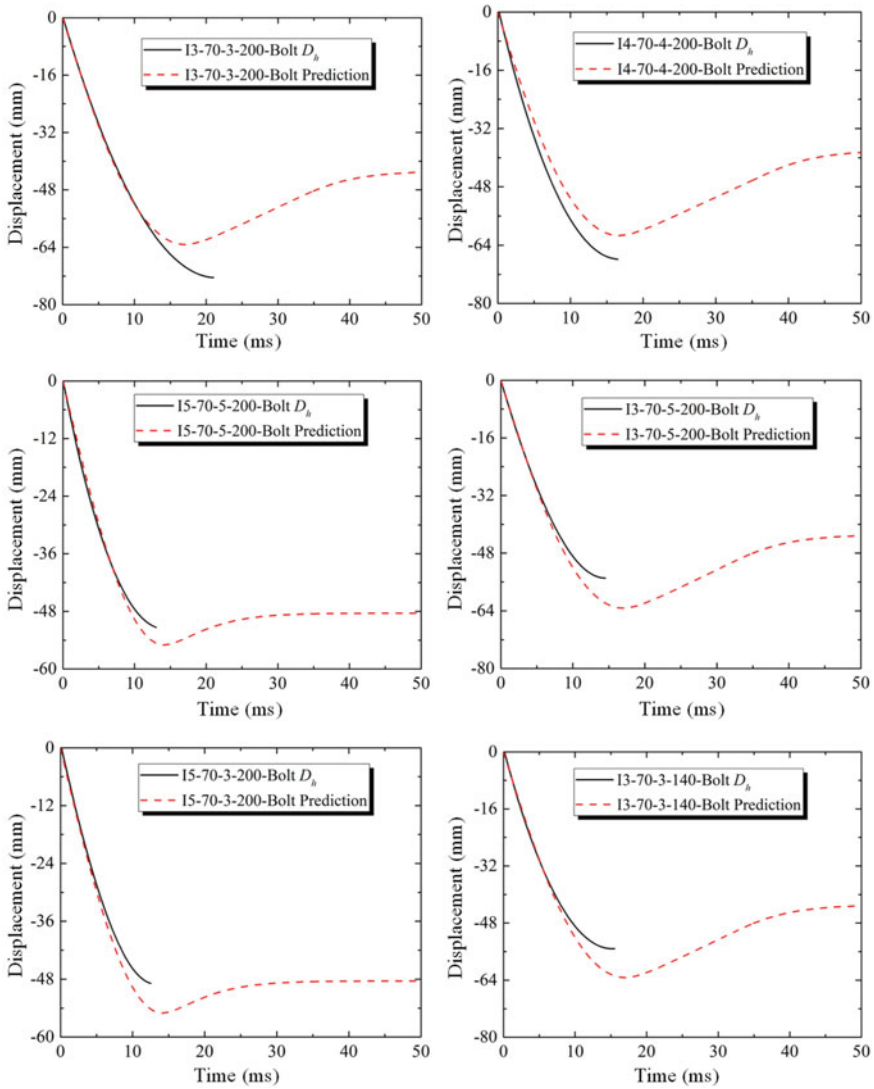
Fig. 7.23 Comparison of displacement–time histories between tests and analytical predictions

The analytical model is found to reasonably predict the displacement response of the CSCS shell. The differences of maximum displacements between analytical-predictions and impact tests are less than 15%. Hence, the proposed analytical model is proven to be acceptable and can be employed as a simple alternative to predict displacement response of the CSCS shell under impact loading.

7.6 Summary

Nine CSCS sandwich shells were tested to investigate their performances under drop-weight impact loading. The FE model of the CSCS shell was also established and verified against the experimental data. The main findings are summarized as follows:

(1) Three failure types of the CSCS sandwich shells under impact load were observed, i.e., Failure type I (plastic deformation of steel plate without fracture), Failure type II (fracture of steel plate) and Failure type III (penetration of steel plate). The thicker concrete core led to more serious failure type (sifting from failure type II to type III). Increasing thickness of steel plates and decreasing spacing of shear connectors could mitigate damage of the CSCS sandwich shell.

(2) Three stages of the impact process were summarized, i.e., inertial stage, loading stage and unloading stage. Both the three failure types showed similar phenomena in the inertial stage and unloading stage. While there were some differences in the loading stage, i.e., the impact force dropped down for the specimens with fracture or penetration of the steel plate.

(3) The impact performances of CSCS sandwich shells with different parameters were analyzed. For the specimens with thicker concrete core, higher inertial peak force and impact resistance, and more serious failure type were observed. By increasing the thickness of steel plate or decreasing the spacing of shear connectors, the specimen showed higher inertial peak force and impact resistance as well as less damage.

(4) The FE model of the CSCS shell was established and verified by comparing the impact force history, displacement history and failure type between the FE-predictions and experimental results. Concrete core was proven to be the main part to dissipate impact energy, followed by the top steel plate and bottom steel plate.

(5) An analytical model based on the equivalent SDOF system was proposed for predicting displacement response of the CSCS sandwich shell under impact loading. The established analytical model was proven to be accurate by comparing the analytical-predictions with test data.

References

Abramowicz W, Jones N (1986) Dynamic progressive buckling of circular and square tubes. Int J Impact Eng 4:243–270

Ali A, Kim D, Cho S G (2013) Modeling of nonlinear cyclic load behavior of I-shaped composite steel-concrete shear walls of nuclear power plants. Nucl Eng Technol 45(1):89–98

Guo Q, Zhao W (2019) Displacement response of steel-concrete composite panels subjected to impact loadings. Int J Impact Eng 131:272–281

Hoff GC (1998) A major research program on steel-concrete-steel sandwich elements. Construction 174:37–88

Huang Z, Liew JYR (2016a) Compressive resistance of steel-concrete-steel sandwich composite walls with J-hook connectors. J Constr Steel Res 124:142–162

Huang Z, Liew JYR (2016b) Experimental and analytical studies of curved steel–concrete–steel sandwich panels under patch loads. Mater Des 93:104–117

Huang Z, Liew JYR (2015a) Nonlinear finite element modelling and parametric study of curved steel–concrete–steel double skin composite panels infilled with ultra-lightweight cement composite. Constr Build Mater 95:922–938

Huang Z, Liew JYR (2016c) Structural behaviour of steel–concrete–steel sandwich composite wall subjected to compression and end moment. Thin-Walled Struct 98:592–606

Huang ZY, Liew JYR (2016d) Steel-concrete-steel sandwich composite structures subjected to extreme loads. Inter J Steel Struct 16(4):1009–1028

Huang ZY, Wang JY, Liew JYR et al (2015b) Lightweight steel–concrete–steel sandwich composite shell subject to punching shear. Ocean Eng 102:146–161

Hallquist JO (2006) LS-DYNA theory manual. Livermore Software Technology Corporation (LSTC). Livermore, California

Leng YB, Song XB, Chu M et al (2015) Experimental study and theoretical analysis on resistance of steel-concrete-steel sandwich beams. J Struct Eng 141(2):04014113

Leng YB, Song XB (2017) Flexural and shear performance of steel-concrete-steel sandwich slabs under concentrate loads. J Constr Steel Res 134:38–52

Liew JYR, Sohel KMA, Koh CG (2009) Impact tests on steel-concrete-steel sandwich beams with lightweight concrete core. Eng Struct 31(9):2045–2059

Lin Y, Yan J, Cao Z et al (2018) Ultimate strength behaviour of S-UHPC-S and SCS sandwich beams under shear loads. J Constr Steel Res 14a9:195–206

Lin Y, Yan J, Wang Y et al (2019) Shear failure mechanisms of SCS sandwich beams considering bond-slip between steel plates and concrete. Eng Struct 181:458–475

Mizuno J, Koshika N, Sawamoto Y et al (2005) Investigation on impact resistance of steel plate reinforced concrete barriers against aircraft impact Part 1: Test program and results. In: the 18th International Conference on Structural Mechanics in Reactor Technology, Beijing, China, 7–12 August 2005

Montague P (1975) A simple composite construction for cylindrical shells subjected to external pressure. J Mech Eng Sci 17(2):105–113

Remennikov AM, Kong SY (2012) Numerical simulation and validation of impact response of axially-restrained steel–concrete–steel sandwich panel. Compos Struct 94(12):3546–3555

Remennikov AM, Kong SY, Uy B (2013) The response of axially restrained non-composite steel–concrete–steel sandwich panels due to large impact loading. Eng Struct 49:806–818

Sohel KMA, Liew JYR (2014) Behavior of steel-concrete-steel sandwich slabs subject to impact load. J Constr Steel Res 100:163–175

Sohel KMA, Liew JYR, Koh CG (2015) Numerical modelling of lightweight Steel-Concrete-Steel sandwich composite beams subjected to impact. Thin-Walled Struct 94:135–146

Timoshenko SP, Woinowsky-Krieger S (1959) Theory of plates and shells. McGraw-Hill, New York

Wang Y, Liew JYR, Lee SC (2015) Theoretical models for axially restrained steel-concrete-steel sandwich panels under blast loading. Int J Impact Eng 76:221–231

Wang Y, Liew JYR, Lee SC (2016a) Ultimate strength of steel–concrete–steel sandwich panels under lateral pressure loading. Eng Struct 115:96–106

Wang Y, Zhai X, Lee SC (2016b) Responses of curved steel-concrete-steel sandwich shells subjected to blast loading. Thin-Walled Struct 108:185–192

Yan C, Wang Y, Zhai X et al (2019a) Experimental study on curved steel-concrete-steel sandwich shells under concentrated load by a hemi-spherical head. Thin-Walled Struct 137:117–128

Yan C, Wang Y, Zhai X (2020a) Low velocity impact performance of curved steel-concrete-steel sandwich shells with bolt connectors. Thin-Walled Struct 150:106672

Yan C, Wang Y, Zhai X et al (2020b) Strength assessment of curved steel-concrete-steel sandwich shells with bolt connectors under concentrated load. Eng Struct 212:110465

Yan J, Zhou W, Zhang X et al (2019b) Interface monitoring of steel-concrete-steel sandwich structures using piezoelectric transducers. Nucl Eng Technol 51:1132–1141

Yan JB, Liew JYR, Zhang MH et al (2016a) Punching shear resistance of steel-concrete-steel sandwich composite shell structure. Eng Struct 117:470–485

Yan JB, Qian X, Liew JYR et al (2016b) Damage plasticity based numerical analysis on steel-concrete-steel sandwich shells used in the Arctic offshore structure. Eng Struct 117:542–559

Yan JB, Xiong MX, Qian X et al (2016c) Numerical and parametric study of curved steel-concrete-steel sandwich composite beams under concentrated loading. Mater Struct 49(10):3981–4001

Yan JB, Zhang W (2017) Numerical analysis on steel-concrete-steel sandwich plates by damage plasticity model: From materials to structures. Constr Build Mater 149:801–815

Zhao W, Guo Q (2018) Experimental study on impact and post-impact behavior of steel-concrete composite panels. Thin-Walled Struct 130:405–413

Zhao W, Guo Q, Dou X (2018) Impact response of steel-concrete composite panels: experiments and FE analyses. Steel Compos Struct 26(3):255–263